

Multiphase turbulent flow explains lightning rings in volcanic plumes

Mie Ichihara ^{1✉}, Pablo D. Mininni ^{2,6}, S. Ravichandran ^{3,6}, Corrado Cimarelli^{4,6} & Chris Vagasky ⁵

Hunga Tonga-Hunga Ha’apai (HTHH), a submarine caldera volcano of the Tonga archipelago, erupted explosively on January 15, 2022. The eruption generated the highest concentration of lightning events ever recorded, producing characteristic ring patterns of electrical discharges concentric to the vent. Here we reproduce the key features of the observations using three-dimensional simulations of buoyant plumes in a stably stratified atmosphere. Our idealized minimal model based on the Boussinesq approximation and heavy particles reveals that the essential mechanism underlying the formation of lightning rings is turbulence-induced particle clustering, which generates structures, favorable conditions for charge concentration by particle collision. We propose that the location, size, and persistence of lightning ring structures can reveal pulsatory activity at the vent that the opaque ash cloud hides from the satellite observation and can be used as a proxy for eruption parameters regulating the generation of hazardous impacts on the environment.

¹Earthquake Research Institute, University of Tokyo, Yayoi, Bunkyo-ku 1130032 Tokyo, Japan. ²Universidad de Buenos Aires, Facultad de Ciencias Exactas y Naturales, Departamento de Física, and CONICET - Universidad de Buenos Aires, Instituto de Física Interdisciplinaria y Aplicada (INFINA), Ciudad Universitaria, Buenos Aires 1428, Argentina. ³Interdisciplinary Programme in Climate Studies, Indian Institute of Technology Bombay, Mumbai 400076 Maharashtra, India. ⁴Department für Geo- und Umweltwissenschaften, Ludwig-Maximilians-Universität München, Theresienstrasse 41, Munich 80333 Bayern, Germany. ⁵Vaisala Inc., 194 S Taylor Ave., Louisville 80027-3024 CO, USA. ⁶These authors contributed equally: Pablo D. Mininni, S. Ravichandran, Corrado Cimarelli. ✉email: ichihara@eri.u-tokyo.ac.jp

Hunga-Tonga Hunga Ha'apai (HTHH), a submarine caldera volcano of the Tonga archipelago^{1–3}, erupted explosively on January 15, 2022, with power unprecedented since the advent of modern instrumental recording^{4–6}. Record-breaking characteristics of this eruption include the production of a 57–58 km tall plume⁷, the umbrella expanding to a diameter of 400 km in <1 h⁸, and the generation of multiple geophysical waves propagating globally through the atmosphere, the ocean, and the solid earth^{4–6,9–11}. Analyses of these geophysical waves suggested multiple bursts in several hours^{5,6,10–12}. Purkis et al.¹³ investigated direct tsunami from the explosive volcanic events that hit the Kingdom of Tonga and identified five blasts in 1 h, of which the last two at 4:18 and 4:56 had larger energy (4 Mt and 15 Mt, respectively) than the first three (0.5 Mt or smaller). They emphasized that explosion sequences derived from the global-scale waves and the near-field events were different. The huge umbrella cloud obscured satellite view of the activity at the vent preventing further constraining of the explosive sequence¹⁴.

Another prominent atmospheric effect caused by this eruption is the highest concentration of lightning events ever recorded, peaking nearly 400,000 strokes over 6 h¹⁵, or above 5000 strokes/min¹⁴. Lightning marked the inception of the eruption and evolved in space and time producing characteristic ring patterns centered over the volcanic vent^{8,16,17} (Fig. 1). Gaps in the volume-filling lightning activity of large supercell storms have been described before^{18,19} and interpreted as due to localized regions of strong updraft within the thunderstorm. However, meteorological lightning discharges have never showed such regular symmetry, extension, or periodicity as those produced during the HTHH eruption. The origin of this phenomenon poses an interesting question, and its answer could also provide useful information on eruption activity.

Here we investigate the hypothesis that particle clustering in the turbulent flow can give rise to the observed lightning ring

structures. We perform three-dimensional numerical simulations of a turbulent plume with solid particles in a stratified atmosphere, considering a simple single-phase incompressible fluid in a linearly stratified atmosphere under the Boussinesq approximation, and passive heavy particles with linear drag to model a particle laden flow (see the ref. ²⁰ for more realistic multiphase plume models). Our aim is to constrain the physical conditions that generate the ring structure in a convective plume, rather than to accurately simulate the HTHH eruption. In order to constrain the physical conditions generating the ring structures, we analyze the relation between turbulence production and particle accumulation (or, indirectly, lightning patterns and volcanic plume parameters). Our model shows that particles' ring structures are determined by the turbulence in the eruptive column and umbrella cloud due to the interaction with the still atmosphere and the turbulent-induced particle clustering, as they generate favorable conditions for charge concentration by particle collision. We show that the extension, persistence and decay of the lightning ring structures can be related to in-plume fluid dynamics parameters otherwise inaccessible through direct measurements and that they can be used as an indicator of successive explosions obscured to satellite observation by the expansion of the plume umbrella.

Background

Volcanic activity. The HTHH submarine caldera has a historic record of violent explosive eruptions often propelled by the interaction of andesitic magma with ocean water^{1,2}. After seven years of repose, HTHH volcano erupted first in mid-December, 2021, with Surtseyan explosion of similar characteristics of those recorded in 2009 and 2014–2015¹⁶. After about a week of pause, the activity resumed on 13 January 2022 (all times and days hereafter are in UTC) producing a 11 km tall plume accompanied

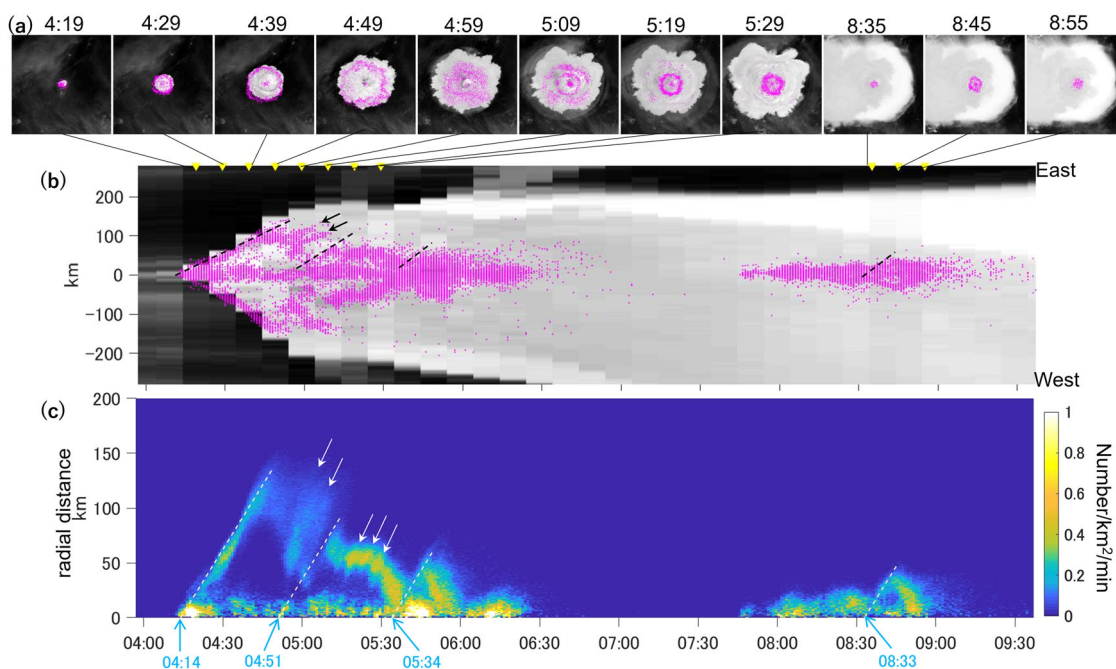


Fig. 1 Observed lightning rings during the January 15, 2022, eruption of Hunga-Tonga Hunga-Ha'apai volcano. **a** Lightning sources (magenta dots) in 1 min from the indicated time superimposed on the temporally nearest Himawari-8 satellite infrared images (downloaded from NICT-Japan and processed at ERI, U-Tokyo). Note that Himawari-8 takes images of the area at 7.5 min after every 10 min (e.g., 4:17.5, 4:27.5, etc.). **b** Temporal variation of the east-west slice (5-km around the center) of the structure like **(a)**. **c** The lightning source number density (counts/km²/min) as a function of time and radial distance. Although Bór et al.¹⁴ presented similar plots for event rate per distance, we show event rate per area to compare the data with our numerical results. Some expanding features are noticed (dashed lines assuming 65 m s⁻¹ and arrows), which are discussed in the “Effects of gravity waves and of particle settling” section.

by intense lightning activity (about 55,000 lightning events, as measured by the Vaisala GLD360 network²¹) clustered around the vent. After 12:00 on 14 January, the eruption became intermittent and the activity temporally declined²². At about 04:00 on 15 January, the first of a series of main explosions started. We discuss next the main explosions (see Fig. 1).

Figure 1 shows the observed lightning ring evolution with the umbrella cloud, as reported previously^{8,14,16,17}. The lightning sources (magenta circles) form a ring, which initially radially expands (Fig. 1a: 4:29–4:49) and diffuses (Fig. 1a: 4:49–5:09). Following, a second ring appears (Fig. 1a: 5:09–5:29) analogous to the first one. The temporal evolution is highlighted in the East-West slices (Fig. 1b) and the lightning number density (count/km²/min) as a function of time and radial distance from the vent (Fig. 1c).

Volcanic lightning generation mechanism. Electrification of volcanic plumes can be achieved mainly through size-dependent triboelectrification of colliding ash particles^{23–25} and additionally through the collisions of hydrometeors formed in situ^{26,27}, the formation rate of the latter being determined by the contribution of water vapor (with either magmatic or external origins) advected in the plume and the enhanced ice nucleation by the presence of volcanic ash^{28,29}. Furthermore, as in the case of submarine eruptions breaching the surface, magma fragmentation by contact with water and consequent water vaporization can add to the electrification of the emerging plume^{30–33}. Lightning discharges are therefore believed to be intimately related to the nature and size of charged particles, their spatial distribution, and collision frequency, so that the lightning rate could provide insights into particle acceleration and turbulence as well as plume extent^{26,27,34–36}. However, in order that lightning rates may be used to infer eruption properties, the mechanisms through which turbulence in the volcanic plumes effects electrification need to be further investigated.

Turbulence is known as a physical phenomenon that mixes fluids and particles carried by a fluid very efficiently. However, under certain conditions, turbulence can “unmix” particles, segregating them in regions or patches with high density. This phenomenon of “preferential concentration” or “clustering” can decrease the effective mean free path between particles, and increase collision rates above the value expected for homogeneous distributions^{37–39}. Here we want to investigate whether turbulence and associated phenomena can give rise to lightning ring structures as those observed at HTHH and other volcanic eruptions.

Plume dynamics. The fundamental dynamics of free-shear flows was modeled by Morton et al.⁴⁰ (hereafter referred to as MT1956). The controlling factor is the entrainment velocity which determines the rate at which non-turbulent ambient fluid is incorporated into the flow of interest. MT1956 postulated that the entrainment velocity is proportional to some characteristic velocity of the flow. Furthermore, their model incorporated a Boussinesq approximation, which is valid when the density difference between the plume and the ambient fluids can be ignored except for its effect on the buoyancy force. MT1956 dealt with both fixed-volume “thermals” and fixed-flux plumes.

Long-lasting eruptions, like the HTHH event, are often modeled as fixed-flux plumes. They are characterized by a constant energy input rate \dot{Q} , which is equivalent with a buoyancy input rate in MT1956. This model shows that the radius, r_p , of a steady maintained plume in an unstratified ambient grows proportionally with its height, z_p , as $r_p \sim z_p \propto t^{3/4}$. A volcanic plume generally rises in a stably stratified environment and stops

rising at its level of neutral buoyancy (LNB). The one-dimensional representation of MT1956 predicts the maximum plume height H to be proportional to $\dot{Q}^{1/4}$.

The fix-volume plume model of MT1956 in a stably stratified medium has been applied to short-duration explosions generating volumes of fluid lighter than the surroundings, the thermals. A thermal having thermal energy Q reaches a height $H \propto Q^{1/4}$ (note that in this relation Q is the instantaneous injection of thermal energy). Regardless of the simplifications, MT1956 and similar models explain the essential behaviors of plumes, either volcanic or non-volcanic, and have become the basis of modern plume models^{41–44}. Once the plume reaches and overshoots its LNB, an umbrella cloud forms as the flow spreads out. Modeled as a gravity current, the umbrella cloud radius, r_c (the square-root of cloud area), is expected to follow $r_c \propto t^{2/3}$ for a fixed-flux plume and $r_c \propto t^{1/3}$ for a fixed-volume plume⁴⁵.

Large volcanic eruptions display both transient and continuous features, with explosions marking the onset of the eruption but also producing pulses during the sustained phase.

Volcanic eruptions are different from buoyancy inputs as the flows are generally high-density and high-velocity jets at the vent. The jets rapidly mix with the ambient air and transfer their thermal and kinetic energy to the buoyancy. MT1956 models do not deal with the dynamics of the jet region, called the “gas-thrust region”⁴⁴. In volcanology, efforts have been made to model this gas-thrust region, incorporating complex effects such as different entrainment mechanisms, supersonic expansion with standing shock waves, internal inhomogeneity, and incomplete thermal equilibration between particles and gas^{44,46–48}. Although the dynamics in the gas-thrust region may have essential influence on the stability/collapse of plumes and the relationship between H and \dot{Q} ^{44,46}, the plume is regarded as a buoyancy-driven convective plume once it gains buoyancy, and the gas-thrust region makes up only a small fraction at the lowest part of the plume^{44,48}.

Other essential factors that deviate volcanic plumes in the convective region from MT1956 models are winds^{49,50} and external surface water^{43,51,52}. The latter is particularly important for strong plumes formed by submarine eruptions, as observed in the HTHH eruption. The net effect of external water on plume dynamics is non-monotonic. If the mass fraction of the surface water entrained is small ($\lesssim 10\%$), the effect of water is to increase the plume buoyancy due to the increase of volume upon evaporation resulting in greater final plume height. However, if too much water is entrained the net effect is a decrease in the plume buoyancy, resulting in smaller final plume heights^{43,51}. Maeno et al.⁵² modified the conventional steady one-dimensional plume model to represent a recent shallow-sea eruption in Japan, where a large fraction of erupted magma remained in the sea as pumice rafts, using its thermal energy to evaporate sea water. Then, a low-density high-energy vapor plume was formed, which reached large H for relatively small \dot{Q} .

Three-dimensional numerical models have been developed to simulate the observed and theoretical plume behaviors in a stratified medium^{41,53–55}. In a simulation of the 2014 eruption of Kelud volcano in Indonesia, Suzuki and Iguchi⁵⁶ showed that expansion of the umbrella cloud radius was consistent with a fixed-flux gravity current model ($r_c \propto t^{2/3}$) after 1000 s, but was much more rapid as $r_c \propto t^{1.07}$ before 1000 s from the eruption onset. The 3D multiphase flow simulations^{20,54} included the gas-particle relative motions due to both inertia and gravitational effects. Although they pointed out the particle clustering due to turbulence, they mainly focused on the large-scale effects like the entrainment coefficient and plume shape. Their simulations also included gas compressibility and demonstrated its effect on the supersonic jet region below the buoyancy region.

While increasingly complex plume models may be more realistic, too many details may obscure the essential mechanisms and factors underlying other observed phenomena. To answer similar questions, Hernandez-Duenas et al.⁵⁷ investigated minimal models for precipitating turbulent plumes. Our study follows their concept to capture the effect of turbulence without relying on subgrid models for inertial range effects at relevant scales.

Results

We conducted simulations of a stably stratified flow, with continuous buoyancy input from a small hot source in the lower part of the domain to generate a turbulent plume, together with the integration of four sets of particles advected by the fluid. The flow is assumed to be incompressible (Mach number equal to zero), the background stratification profile of the atmosphere before the eruption is linear with height (exponential decay at high altitudes is not considered), and particles use a model with linear drag that is valid for small and heavy particles (see “Methods” for all approximations and relevant parameters). Three sets of particles were placed in a thin layer at the bottom of the domain, in such a way that the plume can push particles upward. These sets of particles with decreasing inertia have Stokes numbers of $St = 1$, 10^{-1} , and 10^{-2} , hereafter labeled A, B, and C, respectively (see “Methods” for the definition of the Stokes number). A fourth set of homogeneously distributed particles with $St = 1$ was placed between heights of 10 to 60 km (in the following, “initially suspended particles” or ISP), to study whether particles already present in the atmosphere (e.g., ice crystals, volcanic ash particles and aerosols from preceding eruptions) can cluster as a result of interacting with the turbulence. Except for a simulation discussed later, settling of particles is neglected in all cases. As time progresses, the hot source in the bottom generates a plume of fluid moving upwards, that also advects the different sets of particles. This plume first overshoots the LNB at $t \approx 2$ min, and then spreads horizontally with the hot fluid asymptotically reaching the LNB.

Figure 2 shows a three-dimensional visualization of different species of particles 43 min after the initialization of the plume. In the side view, the three million particles with $St = 10^{-2}$ are shown together with the flow squared vorticity in half the domain. In the top view, particles with $St = 10^{-2}$ and 1, and the ISP, are shown together with the squared vorticity. Particles with lesser inertia (smaller St) follow the flow more closely, and move further out radially, while particles with larger St move further up in the central column, and to a lesser degree radially. However, in both cases an annular region with similar radius can be identified where the particle densities are substantially larger. The annular regions with larger density can also be identified for the ISP. These regions of strong particle accumulation correlate with regions with strong turbulence, as shown later.

Figure 3a shows the particle densities as a function of the radius, $n_i(r)$, for all particle species considered (i.e., for $i = A, B, C$, or ISP) at $t = 43$ min. As a reference, we also show the profile of the squared vorticity $\omega^2(r)$, to quantify the strength of turbulence as a function of the radial distance from the central column. All particles starting from the bottom of the domain at $t = 0$ (species A, B, and C) have a maximum in the central column, and another maximum at $r \approx 40$ km, where the vorticity and turbulence intensity are maximum (comparisons with the turbulent kinetic energy yield similar results). The particles initially suspended at $t = 0$ (ISP) also display rings with maximum accumulation at $r \approx 25$ and ≈ 40 km, the curves tending to the mean homogeneous value of the density at large distances, where the particles are undisturbed (i.e., $n_i(r) \approx \langle n_i \rangle$ for large r).

The density of particles provides a first proxy to possible enhancements in the number of collisions, which can in turn result in enhanced electrification only if the accumulation of the different particles takes place in the same places (note that electrification mostly results from collisions between particles with different sizes and masses). As the numerical integration of realistic numbers of particles in a domain of 188 km of length is out of reach of today’s computational capabilities, direct computation of collisions is unfeasible. We can instead obtain an estimation of the probability of collisions between species from the cross-correlations of densities of different sets of particles⁵⁸. Or, from kinetic theory, we can expect the number of collisions between different species of particles to be proportional to the product of the densities times their characteristic velocities,

$$N_{i,j} = n_i n_j (v_i v_j)^{1/2}, \quad (1)$$

where v_i is the r.m.s. velocity of the particles’ species i (estimations using the particles relative velocities yield similar results as the ones discussed below, as all particles have similar r.m.s. velocities, see “Methods” for details). This quantity as a function of the radius, and its normalized value is shown in Fig. 3b at $t = 43$ min for species A and C (i.e., for particles with $St = 1$ and 10^{-2}) and for ISP and species C (i.e., for the initially suspended larger particles, and the smaller particles with $St = 10^{-2}$, respectively), as well as for A-A and C-C cross-correlations. All cases show a maximum near the central column, and a second maximum at $r \approx 40$ km. The most prominent of these maxima are those for $N_{A,C}$ and $N_{ISP,C}$. Note that for electrification, the interest is in the interactions between species with very different sizes (and, in the case of ice particles, growth rates⁵⁹).

The foregoing results are for $t = 43$ min. With time, the radius of the region of accumulation of particles (and of large cross-correlation between all species) fluctuates, but with a well-defined mean radius, even as the plume continues expanding. Figure 4a shows the evolution of $n_A(r)$ (with $St = 1$) as a function of time in color, together with the radius of the “cloud,” where the border of the structure is defined as the radius at which the density of the particles C (with $St = 10^{-2}$, i.e., the particles with less inertial and better coupled to the flow) drops below a small threshold. The figure also shows the position of the ring-like region of preferentially larger collision rates, defined as the position of the second most prominent maximum of the cross-correlation $N_{A,C}(r)$ shown in Fig. 3b. Note that the cloud continues to expand with time, while this ring fluctuates around a radius that correlates with the region of maximum turbulence intensity. As in the observations (Fig. 1), we see in Fig. 4a a region near the center of the domain (at $r \approx 10$ km) with a large density of particles, with “fingers” of large density that expand radially linearly in time. The ring (in particular, the second peak in $N_{A,C}$) is recreated many times, also evolving approximately linearly in time in between and fluctuating around $r \approx 40$ km. Figure 4b shows the radius of the cloud and of this ring in log-log scale, with two power laws indicated only as a reference.

Discussion

We showed that turbulence in the buoyant plume can accumulate particles and increase their collision probability in the central core and a ring-like region, generating an annular gap between the core and the ring. Our simulations also revealed that the ring-like region initially expands with the plume and fluctuates at ≈ 40 km while the plume edge continues to move radially outwards. Comparison of time scales in cluster formation and particle dynamics (see the “Effects of gravity waves and of particle settling” section) also indicates that turbulence is dominant in the horizontal evolution of the particles, while stratification plays a

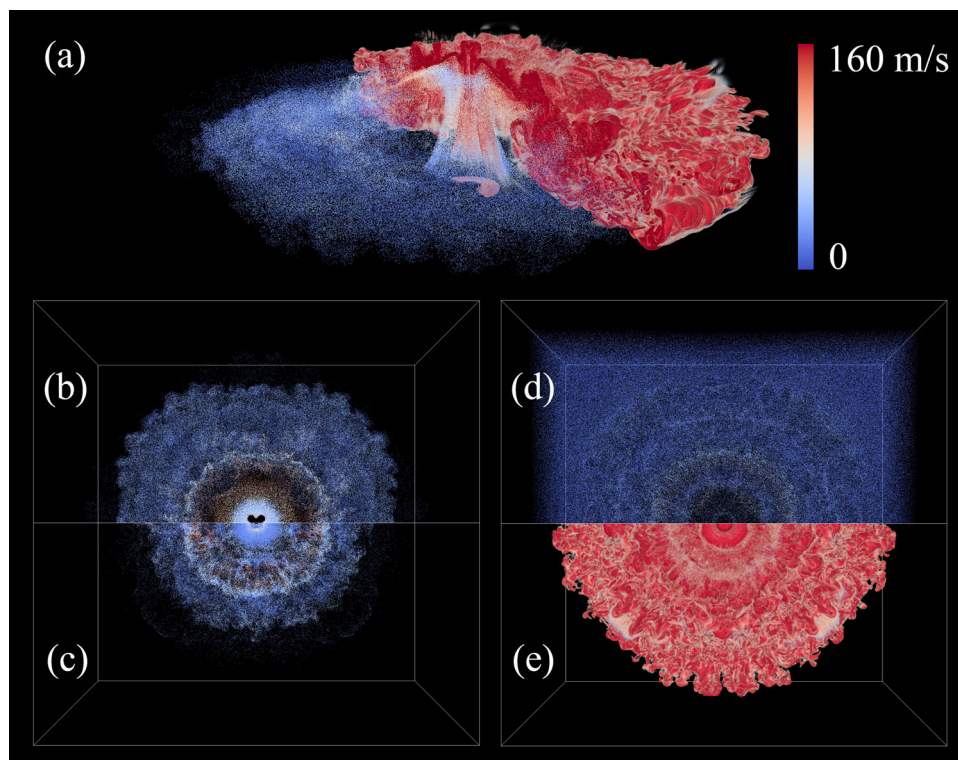


Fig. 2 Visualization of the three-dimensional numerical results. **a** Three-dimensional rendering of the flow squared vorticity (in red, shown in half the domain), together with three million particles in colors with $St = 10^{-2}$ (species C). The color bar indicates the particles velocity in all panels. Particles seen from the top with **b** $St = 10^{-2}$ (species C), and **c** $St = 1$ (species A). Note the ring with strong accumulation of both species, and with large particles velocities. **d** Particles with $St = 1$, for the case initially suspended homogeneously (ISP). **e** Flow squared vorticity, seen from above. All images correspond to $t = 43$ min.

role in further confining the particles vertically (see also related discussions by Van Eaton et al.¹⁷).

The model solved here is a simplified set up for a turbulent plume in a dry and linearly stratified Boussinesq medium, with non-interacting (one-way coupled) point and heavy inertial particles. Modification and new formation of particles due to vapor condensation is therefore not captured by the model, while it still mimics in a simple way the presence of particles already suspended at the time of plume injection, such as ice crystals and older ash particles. It also considers a steady source for the plume, while source parameters in a volcanic eruption are time-dependent. The flow compressibility effects are not considered, either, though they may influence the plume behavior^{20,54}. Thus, care must be taken when comparing the simulation parameters with the observations.

In spite of these limitations, we believe the ring-like structures obtained by our simulations may be linked to the lightning ring observed during the HTHH eruption. Below we discuss the relevance and implications of the linkage.

Thunderstorm lightning vs. volcanic lightning ring. Bôr et al.¹⁴, who reported detailed observations of HTHH lightning, compared the lightning rings with a very active supercell during thunderstorms and linked them with updraft surges. The lack of lightning activity within confined regions of thunderstorm clouds (“lightning holes”) has been observed in supercell systems^{18,19} and has been interpreted as an indicator of severe weather conditions. Such lightning holes are known to drift with time, coinciding with regions of strong updraft within the cloud. Conversely, in the HTHH plume the central region over the vent, where we expect the strongest updrafts, is almost continuously

marked by lightning activity (Fig. 1, except a temporal break between 06:30 and 7:45), while lightning ring structures (and the associated annular gaps) appear and dissolve periodically in a persistently concentric region. Note that strong and episodic updraft surges are however another possible source of inhomogeneities in particle distribution.

Non-inductive electrification of volcanic plumes and thunderclouds is in large part caused by collisions between particles with different sizes^{23,58–61}. However, when particles are not homogeneously distributed, the number of collisions can be strongly dependent on their relative position. We showed that the buoyant plume can accumulate particles and increase their collision probability in the central core (radial distance within 20 km from the source) and a ring-like region, generating an annular gap between the core and the ring (Fig. 3). Our simulations also revealed that the ring-like structures reached similar radii for very different sizes (i.e., different Stokes numbers), ≈ 40 km in the calculated cases.

Effects of gravity waves and of particle settling. The formation of the ring can be caused by turbulent inertial clustering, or associated to oscillations caused by gravity waves¹⁷. It is not easy to disentangle these effects, but our approach allows us to study the dynamics of each individual particle. Figure 5 shows the frequency power spectrum of the particles’ velocities for species C in the umbrella cloud. The x and z components of the velocity are considered separately. Both components display a range of frequencies compatible with a Kolmogorov spectrum, but v_z has a peak near the Brunt-Väissälä frequency, which corresponds to the lowest frequencies of gravity waves. The spectrum of v_x displays instead excitations at lower frequencies. As a reference,

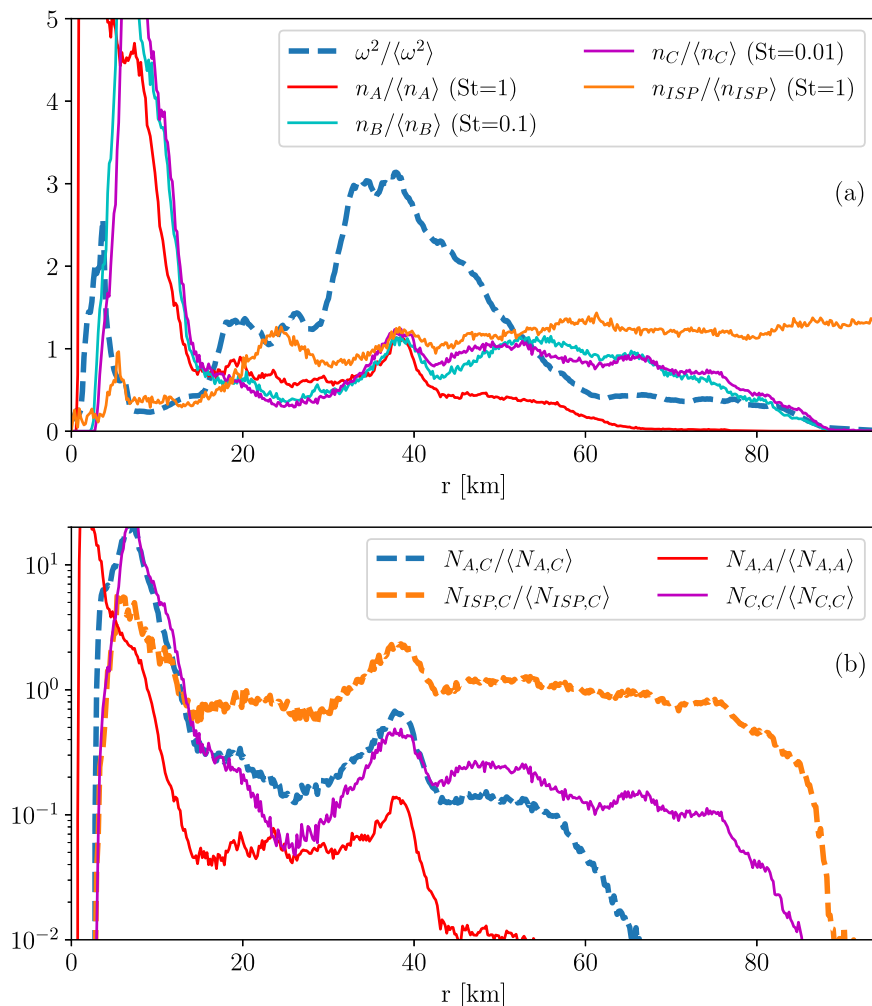


Fig. 3 Radial profiles of parameters relevant to lightning generation. **a** The squared vorticity and the density of particles of each species, normalized by their respective mean values. All quantities have a maximum near the center of the domain, and another around ≈ 40 km. **b** Cross-product of the densities of particles times the square of their r.m.s. turbulent velocities. Quantities are normalized by their mean values, and are considered as a proxy for the number of collisions. Note the peaks at $r\approx 40$, especially for the pairs of species A and C, and ISP and C. All plots correspond to $t=43$ min.

frequencies of $\approx 3 \times 10^{-3} \text{ s}^{-1}$ correspond to the turbulent turnover time of eddies of size of ≈ 20 km. This indicates that while gravity waves in the simulations can enhance particle accumulation through vertical confinement and oscillations with a period of ≈ 100 s (the inverse of the Brunt-Väissälä frequency), the horizontal displacements, which are the essential feature of the lightning rings, are dominated instead by turbulent motions with slower time scales.

We also discuss here the effect of gravity and settling in the clustering of particles, which so far were neglected. Species B and C have smaller settling velocities than the flow turbulent velocity (see “Methods”), and adding gravity has small effects on particle densities (except for a small fraction of particles in regions of small fluid velocity that settle). For species A, adding gravity still results in the formation of a ring with larger particle density around $r\approx 40$ km, while it also increases clustering. This is shown in Fig. 5, which shows the particle density with and without settling of particles. Interestingly, while gravity makes particles in calmer regions of the umbrella cloud to settle, particles in regions with strong turbulence remain suspended and cluster even more.

The expansion behavior of the ring structures and implications to volcanic activity. The simulation captured the basic expansion

behavior of a plume in a stratified medium. A dry plume in a non-stratified medium has a lateral velocity proportional to the vertical velocity, both varying as $t^{-1/4}$, so that the plume radius, r_p , grows like $t^{3/4}$ (see the “Plume dynamics” section). In a stratified medium, r_p is expected to grow faster than $t^{3/4}$. Once the plume hits the LNB, it spreads out as a gravity current, and the umbrella cloud radius, r_c , grows. We see an expansion (mainly r_c) starting proportional to t and decelerating as $t^{0.7}$ and then $t^{0.4}$ in both simulations (Fig. 4) and the HTHH eruption⁸. The expansion of $t^{0.7}$ is consistent with the model for r_c as a gravity current spreading horizontally after a steady plume in a stratified medium⁴⁵ reaches the LNB. The initial expansion as $\propto t$ may indicate that the supply rate is accelerating.

At the inception of the HTHH eruption, the lightning ring marks the extension of the expanding umbrella cloud, as both features travel at the same constant radial velocity in the early stage of umbrella growth⁸ (see Fig. 1). In our simulation, the ‘ring’ of particle and vorticity concentration exhibited similar expansion behaviors (Fig. 4). It is worth noting that clustering of particles in turbulence is different for plumes injected in isotropic and homogeneous media than for stratified media, as found in the atmosphere⁶². The density stratification of the medium is thus essential to reproduce the generation and growth of ring-like structures (see a sketch of the process in Fig. 6). On the other

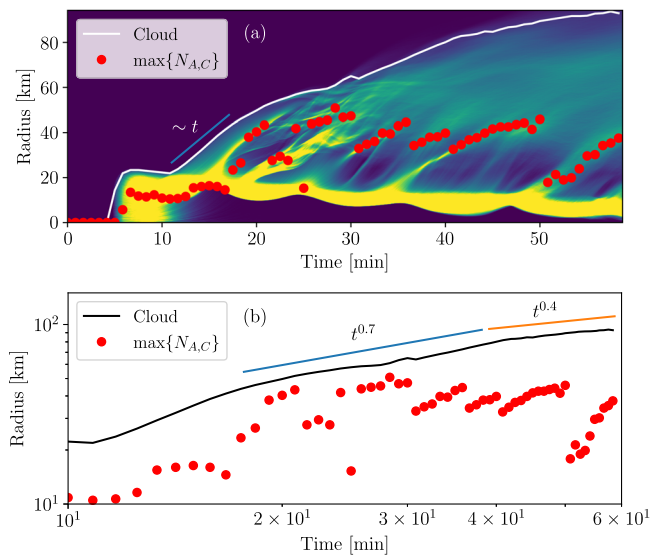


Fig. 4 Evolution of the radial structure in a plume. **a** The density of species A, $n_A(r, t)$, showing a prominent peak near the axis of the plume and multiple radiating ‘fingers’. The white solid line indicates the border of the cloud as a function of time, and the red dots indicate the position of the second maximum observed in Fig. 3 as a function of time. A linear time dependence is indicated by the straight blue line at early times, which also serves as a reference for the evolution of the rings. **b** The radius of the cloud and of $\max\{N_{A,C}\}$ as a function of time in log-log scale. Two power laws at later times are shown as ref. ⁴⁵ (see also the HTHH case⁸). Note that while the cloud keeps expanding in time, the annular structure fluctuates around a mean radius of ≈ 40 km.

hand, the ring expansion speed is $\approx 65 \text{ m s}^{-1}$ in both simulation (Fig. 4a) and observation (Fig. 1c), which is much slower than the gravity waves (horizontal phase speeds of 240–270 m s^{-1} in the HTHH eruption⁵, and of $\approx 200 \text{ m s}^{-1}$ in the simulation for horizontal scales of ≈ 20 km).

The spatial-temporal distribution of lightning activity in the HTHH plume shows multiple successive radial expansions of lightning ring structures as highlighted by the dashed lines and arrows in Fig. 1b and c. Some of these alignments originate from the vent area (dashed lines). The others appear at a distance from the vent and propagate further away (arrows). The numerical result also exhibits outward movement of $\max\{N_{A,C}\}$ (red circles in Fig. 4); the first one from the center and the subsequent ones at a distance of about 40 km. Note that the numerical simulation assumes a constant flux after the onset, thus implying that not all expanding rings necessarily indicate new flow injection nor unsteady mass discharge rate at the source. On the contrary, rings originating from the vent area (in the observational data) likely mark the onset of a new explosion. Based on these observations and the qualitative behavior in the simulations, we can infer that significant explosions at HTHH occurred in several minutes around 4:14, 4:51, 5:34, and 8:33 (Fig. 1c). Interestingly, the first three times are comparable with the observed major earthquakes at HTHH, resolved by the global seismic network at 4:07:53–4:14:45 (two M4.7 events and one M5.8), 4:40:37 (M4.8) and 5:30:17 (M4.7)⁶³. Also, the first two times may be associated with the two energetic blasts at 4:18 and 4:56, inferred from the direct tsunami hitting the Kingdom of Tonga¹³. The last one may be associated with the strong eruption detected by infrasound and hydroacoustic stations at 8:31¹¹. Around 6:00, before 8:00, and around 8:15, smaller explosions might have occurred and produced rings not resolvable in the current dataset.

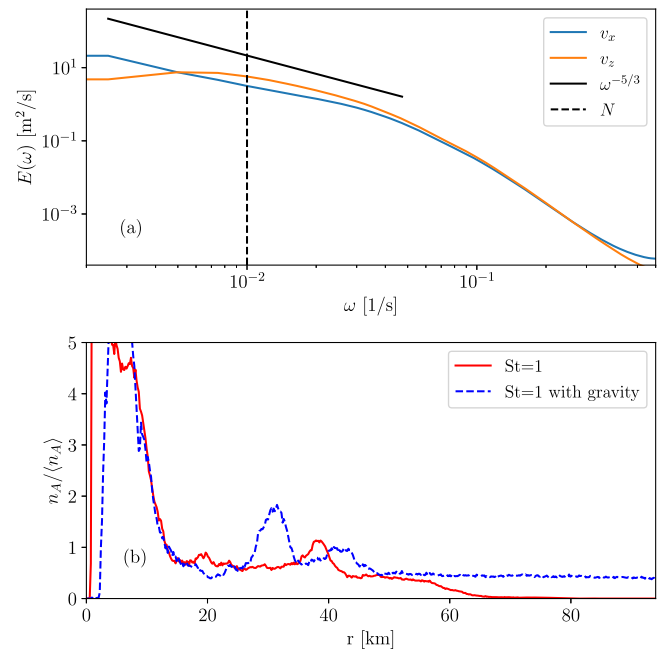


Fig. 5 Gravity effects. **a** Power spectrum of the particles’ velocities for species C, for the x and z components of the velocity. A Kolmogorov spectrum is shown as a reference. The vertical dashed line indicates the Brunt-Väisälä frequency. **b** Density of particles (normalized by the mean density) for species A 40 min after the start of the simulation, with and without gravity.

Conclusions

Our numerical simulations for a buoyant plume in a linearly and weakly stratified medium under the Boussinesq approximation with heavy passive point particles have shown that the turbulent clustering mechanism works to concentrate particles in regions of high turbulence intensity surrounding the updraft, in the ring, and in the umbrella cloud (Fig. 6). A high probability of particle collisions is expected in these regions from kinetic theory (Fig. 3). We believe our simulations capture the essential mechanism underlying the lightning ring observed in large volcanic eruptions, including the recent HTHH eruption.

Our minimal simulations are able to reproduce the observed radial expansion of the umbrella cloud as well as the oscillations of the lightning ring. While both umbrella cloud and lightning ring initially expand together as $\propto t$, later on the umbrella expands as $\propto t^{0.7}$ and the lightning ring repeatedly expands and contracts around a fixed radial distance. Most remarkably, our simulation shows that expansion and contraction of the lightning ring happens even if the buoyancy flux at the source remains constant. Based on the results, we distinguish the observed lightning ring expansions due to new explosions from those due to spontaneous fluctuations, and infer the occurrence of significant explosions in several minutes around 4:51, 5:34, and 8:33 UTC on 15 January 2022, otherwise obscured by the expanding plume and umbrella cloud from the primary explosion around 4:14.

Numerical models and observations of volcanic plumes have advanced significantly in recent years, and more precise and detailed volcanic lightning data are becoming available. This study proposes a possible mechanism for the formation and evolution of lightning rings in volcanic plumes. Incorporating this mechanism into numerical models that include more realistic conditions (e.g., the presence of vapors, realistic atmospheric conditions, the supersonic injection of hot material at the source, and non-steady mass discharge), may allow estimation of

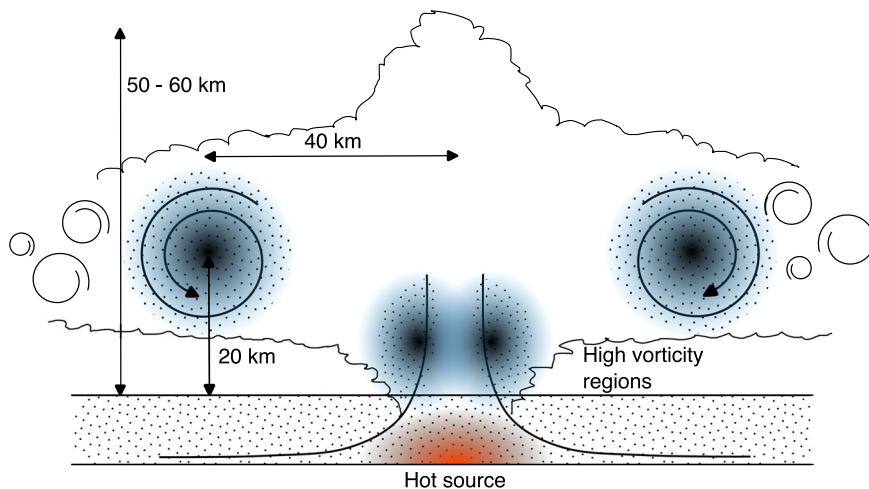


Fig. 6 Schematic diagram of the formation of the plume in the simulation and of the resulting particle clustering. The buoyancy source at the bottom of the domain, shown in red, generates the plume. Vorticity, and turbulence, is stronger in two regions: in the outer region of the ascending jet, where velocity gradients are large, and in an annular region with radius of ≈ 40 km. These two regions of high vorticity correspond to regions of particle clustering for all particles considered. Collisions between these particles could then result in strong electrification of these regions. In the simulations the accumulation of particles is seen above 10 km.

eruption parameters from observations of cloud and lightning dynamics in the future. We emphasize that tracking lightning rings in volcanic plumes is particularly effective in inferring not only the opening explosive episode of a volcanic eruption but also subsequent explosive pulses during its course. For the HTHH eruption, uncovering this sequence is essential to understanding when and how disastrous events like tsunamis, damage to submarine cables, and caldera collapse occurred.

Methods

Numerical simulations and approximations. The flow is described by the Boussinesq equations

$$\partial_t \mathbf{u} + \mathbf{u} \cdot \nabla \mathbf{u} = -\nabla(p/\rho_0) - (g/\rho_0)\rho' \hat{z} + \nu \nabla^2 \mathbf{u}, \quad (2)$$

$$\partial_t \rho' + \mathbf{u} \cdot \nabla \rho' = (\rho_0 N^2/g)\mathbf{u} \cdot \hat{z} + \kappa \nabla^2 \rho' + s, \quad (3)$$

where \mathbf{u} is the incompressible fluid velocity ($\nabla \cdot \mathbf{u} = 0$), and ρ' is the mass density fluctuation around the background linear stratification

$$\rho = \rho_0 + (d\bar{\rho}/dz)(z - z_0) + \rho'. \quad (4)$$

In these equations ρ_0 is the reference fluid density at the reference height z_0 , $d\bar{\rho}/dz < 0$ is the uniform background density gradient (with the convention of $z > 0$ upwards), \hat{z} is a unit vector along the z -axis, g is the acceleration of gravity, p is the correction to the hydrostatic pressure, ν is the kinematic viscosity, κ is the diffusivity, s is a source of density fluctuations, and N is the Brunt-Väisälä frequency. In terms of these parameters, $N^2 = -(g/\rho_0)(d\bar{\rho}/dz)$. The kinematic viscosity was chosen to have the Kolmogorov dissipation scale $\eta = (\nu^2/\langle \omega^2 \rangle)^{1/4}$ well resolved (i.e., larger than the smallest scale resolved by the simulation), where $\omega = \nabla \times \mathbf{u}$ is the vorticity. Note that the r.m.s. value of the vorticity defines the Kolmogorov dissipation time as $\tau_\eta = \langle \omega^2 \rangle^{-1/2}$. We also assume the turbulent Prandtl number is of order unity and use $\kappa = \nu^{64}$.

The incompressible Boussinesq equations can be rewritten using a change of variables for the density fluctuations, $\zeta = g\rho'/(\rho_0 N)$, in such a way that only ν , κ , and N must be prescribed (see below). The correction to the hydrostatic pressure per unit mass density, p/ρ_0 , is obtained from the incompressibility condition, $\nabla^2(p/\rho_0) = -\nabla \cdot (\mathbf{u} \cdot \nabla \mathbf{u} + N\zeta\hat{z})$. Thus, the gas

thermodynamics is decoupled from the evolution of \mathbf{u} and ρ' , and not considered in the time evolution of our model. The reference fluid density ρ_0 can also be chosen arbitrarily. We note that the Boussinesq approximation with linear density variation is not strictly valid for flows deeper than a fraction of the density scale height, $H_p = gN^{-2}$. Better models can be obtained using, e.g., the anelastic approximation. However, we are interested in a minimal model for lightning ring formation in the umbrella cloud, and follow similar approximations as those used in the study of moist convection⁵⁷.

The source s in Eq. (3) is a localized Gaussian ellipsoid of light (hot) fluid at the bottom of the domain, in order to generate a turbulent plume in the stratified flow. A buffer region was left below the source to have fluid at rest and prevent possible artifacts associated to the periodic boundary conditions (the simulation was also stopped before a strong large-scale circulation with the size of the domain was excited by the periodic boundary conditions). The amplitude of the source is constant in time and was set to have in the steady state typical upward velocities in the center of the plume as those in an eruption.

Particles in the simulations satisfy the heavy point particle approximation of the Maxey-Riley equation⁶⁵,

$$\frac{d\mathbf{v}}{dt} = \frac{1}{\tau_p} [\mathbf{u}(\mathbf{x}_p, t) - \mathbf{v}] - g \left(1 - \frac{\rho}{\rho_p} \right) \hat{z}, \quad (5)$$

where τ_p is the particles' Stokes time, \mathbf{v} is the particle velocity, $\mathbf{u}(\mathbf{x}_p, t)$ is the fluid velocity at the particle position \mathbf{x}_p , ρ_p is the particle density, and $\rho/\rho_p \approx \rho_0/\rho_p$. This equation is valid for small particles such that the Reynolds number of the particles satisfies $Re_p = v_s d_p / \nu < 1$, where $v_s = |\mathbf{v} - \mathbf{u}|$ is the slip velocity and d_p is the particles' diameter. For small heavy spherical particles the particles' Stokes time and radius are related by $\tau_p = 2\rho_p d_p^2 / (9\nu\rho_0)$. Under these approximations, the settling velocity of the particles (when the fluid is at rest) is $w \approx g\tau_p(1 - \rho_0/\rho_p)$ ⁶⁶. In all simulations we neglected the effect of gravity and the settling velocity, except for one simulation discussed in the "Effects of gravity waves and of particle settling section".

Equations (2), (3), and (5) were solved numerically with a high-order parallel pseudo-spectral method and high-order interpolation schemes using the GHOST code⁶⁷. Three-dimensional renderings of vector fields and particles were done

using VAPOR⁶⁸. Our simulations solve a stably stratified fluid initially at rest, in a periodic domain of size $L \times L \times H = 188 \times 188 \times 94 \text{ km}^3$. The spatial resolution of all simulations shown in the present study is $1024 \times 1024 \times 512$ grid points. We also performed simulations using $512 \times 512 \times 256$ and $256 \times 256 \times 128$ grid points (with larger values of ν and κ , and smaller values of τ_p) to ensure the results reported here had converged, and did not depend significantly on the spatial resolution and values of viscosity and diffusivity used in the simulations.

Dimensional fluid and particle parameters. The background density stratification in the fluid is fixed by the Brunt-Väisälä frequency, which in the simulations is set to $N = 0.01 \text{ s}^{-1}$. This results in the lowest period of the gravity waves of $\approx 100 \text{ s}$. This value is realistic for stable atmospheric conditions⁶⁹, including the atmosphere above HTHH⁵. The buoyancy source is put at the bottom of the domain creating an upward speed of 150 m s^{-1} . The r.m.s. turbulent velocity in the entire domain at late times is $U \approx 26 \text{ m s}^{-1}$ (note that this value is different from the r.m.s. turbulent velocity in the umbrella cloud, discussed below). Together with the choice of N , the Froude number (a dimensionless measure of the level of atmospheric stratification) results $Fr = U/(LN) \approx 0.01$, where $L = 188 \text{ km}$.

The energy input rate per unit of mass is $\varepsilon = 1.2 \text{ W kg}^{-1}$, which results in a total energy input rate of $\dot{E} = \varepsilon \rho_0 V_s \approx 1.6 \times 10^{12} \text{ W}$, where V_s is the volume of the Gaussian source (with a vertical dispersion of 2.8 km and a horizontal dispersion of 5.6 km) and $\rho_0 = 1.225 \text{ kg m}^{-3}$ is the density of air at sea level. This energy release rate is comparable with an eruption with a mass discharge rate of $2 \times 10^8 \text{ kg s}^{-1}$ assuming a heat capacity of 1000 J kg^{-1} and an excess temperature of 800 K (see a discussion of the energy budget below).

The flow r.m.s. turbulent velocity in the umbrella cloud is $u_{\text{rms}} = 61 \text{ m s}^{-1}$. For the spatial resolution of $1024 \times 1024 \times 512$ grid points, the Kolmogorov microscales are the dissipation time $\tau_\eta = 35 \text{ s}$ and the dissipation scale $\eta = 115 \text{ m}$. The velocity at the dissipation scale is $u_\eta = 3.2 \text{ m s}^{-1}$. With the definitions given in the “Numerical simulations and approximations” section, $\nu = \eta^2 / \tau_\eta = 378 \text{ m}^2 \text{ s}^{-1}$. The viscosity and Kolmogorov scales are large compared with realistic values in volcanic eruptions, where typical values can be as small as $\eta \gtrsim 10 \mu\text{m}$ and $\tau_\eta \gtrsim 10 \mu\text{s}$ ²⁰. Note that explicitly resolving a dissipation scale of $\approx 2 \text{ cm}$ or less would require an increase by more than a factor of 5000 in the linear spatial resolution in each direction.

From these values we can estimate a fluid Taylor microscale $\lambda = u_{\text{rms}}(15/(\omega^2))^{1/2} \approx 8.2 \text{ km}$, and a buoyancy (or vertical stratification) length scale $L_B = u_{\text{rms}}/N \approx 6.1 \text{ km}$. The Taylor Reynolds number then is $R_\lambda = u_{\text{rms}}\lambda/\nu = 1360$. This Reynolds number characterizes turbulent intensity in the inertial range scales of the umbrella cloud.

Volcanic particles (water droplets, ice particles, and other particles in volcanic eruptions) have Stokes numbers St between 10^{-4} to 10^4 ^{24,54}, where St is defined as the ratio of τ_p to some characteristic flow time. The choice of the characteristic flow time is different among studies: Esposti Ongaro and Cerminara⁵⁴ used the large eddy turnover time of a turbulent plume, Gaudin and Cimarelli²⁴ used the vent diameter divided by the jet velocity, and Cerminara et al.²⁰ comparatively used the typical eddy turnover time in the jet at the vent and the turnover time at the Taylor scale in the convective plume. In studies of turbulence it is a common practice to use the Kolmogorov dissipation time as the characteristic time⁷⁰, and thus here we use

$$St = \tau_p / \tau_\eta. \quad (6)$$

Table 1 Typical parameters of the different species of particles.

Species	A	B	C
St	1	0.1	0.01
τ_p [s]	35	3.5	0.35
d_p [m]	$252(\rho_0/\rho_p)^{1/2}$	$79.8(\rho_0/\rho_p)^{1/2}$	$25(\rho_0/\rho_p)^{1/2}$
d_p/η	$2.2(\rho_0/\rho_p)^{1/2}$	$0.69(\rho_0/\rho_p)^{1/2}$	$0.22(\rho_0/\rho_p)^{1/2}$
d_p/λ	$0.03(\rho_0/\rho_p)^{1/2}$	$0.009(\rho_0/\rho_p)^{1/2}$	$0.003(\rho_0/\rho_p)^{1/2}$
v_{rms} [m/s]	62	62	62
v_s [m/s]	3.4	3.3	3.3
Re_p	$2.3(\rho_0/\rho_p)^{1/2}$	$0.73(\rho_0/\rho_p)^{1/2}$	$0.23(\rho_0/\rho_p)^{1/2}$
w [m/s]	$377(1 - \rho_0/\rho_p)$	$37(1 - \rho_0/\rho_p)$	$3.7(1 - \rho_0/\rho_p)$
w/u_{rms}	$6(1 - \rho_0/\rho_p)$	$0.6(1 - \rho_0/\rho_p)$	$0.06(1 - \rho_0/\rho_p)$

Initially suspended particles (ISPs) have the same parameters as species B. $St = \tau_p/\tau_\eta$ is the Stokes number (with τ_η the Kolmogorov time), τ_p is the Stokes time, d_p is the particles diameter, d_p/η is the particles diameter in units of the Kolmogorov scale, d_p/λ is the particles diameter in units of the Taylor scale, v_{rms} is the particles r.m.s. velocity, v_s is the slip velocity (measured in the particles that neglect gravity), Re_p is the Reynolds number of the particles, w is the settling velocity, and w/u_{rms} is the settling velocity in units of the fluid r.m.s. velocity.

Larger and heavier particles correspond to larger values of τ_p and of St . As already mentioned, the approximations made in Eq. (5) are reasonable for small volcanic particles with small enough St . Therefore, we considered particles with $St = 10^{-2}$, 10^{-1} , and 1. As a reference, and to compare with previous studies, our Stokes numbers should be multiplied by ≈ 0.26 to obtain Stokes numbers based on the eddy turnover time at the Taylor scale as reported in ref. 20, and by ≈ 0.1 to obtain Stokes numbers based on the large eddy turnover time at the umbrella cloud. We verified that simulations with $St = 5$ or larger require consideration of at least the settling velocity in Eq. (5)⁶⁶, and perhaps also nonlinear drag effects²⁰.

We considered 4 sets of particles in the simulation, each set containing 3 million particles. Particles are non-interacting: they are affected by the fluid but they do not affect the fluid back, and they do not interact between themselves. Three sets (with $St = 1$, 10^{-1} , and 10^{-2} , i.e., with decreasing inertia) have as initial condition all the particles at rest, homogeneously distributed in a thin layer at the bottom of the domain (labeled, respectively, as species A, B, and C). As the plume develops, particles in this thin layer are advected upwards with the fluid. A fourth set (with $St = 1$) has the particles initially distributed between $z = 10$ and 60 km homogeneously (labeled as “initially suspended particles” or ISP). The aim of this set is to identify whether the turbulent plume can also generate clustering of particles already present in the atmosphere before the eruption, such as small ice particles. Finally, we also performed simulations of species A but considering gravity.

Table 1 shows the typical parameters for all species of particles. While particle radius and times are unrealistic for small particles in an eruption, their ratio to the Kolmogorov scales (as measured by St and d_p/η) are more realistic. As already mentioned, we verified that increasing the spatial resolution from $256 \times 256 \times 128$ to $1024 \times 1024 \times 512$ grid points while keeping these ratios fixed provides convergent results. Particles are also smaller than the Taylor scale in all cases, ensuring that their dynamics are sensitive to inertial range turbulence effects, the main objective of this study. Note also that for particles in the umbrella cloud $\rho_0/\rho_p \ll 1$, and thus the Reynolds number of the particles satisfies $Re_p < 1$ in all cases, thus justifying the assumptions in Eq. (5) needed for linear drag to be a good approximation⁵³. Finally, the settling velocity is smaller than the fluid r.m.s. velocity in all cases except for particles A⁶⁶. The effect of gravity on these particles is discussed in the “Effects of gravity waves and of particle settling” section.

Energy budget in the numerical simulations. We finally present the detailed derivation and estimation of the energy input rate in the numerical simulations, to allow comparisons with typical parameters in volcanic eruptions. The source in the Boussinesq equations is a fluid mass (or thermal) source, and energy is injected as potential energy that can then be converted to kinetic energy by the system dynamics.

The evolution of the fluid density is given by Eq. (3). We can assume the velocity in the vicinity of the source and near the bottom boundary to be $\mathbf{u} \approx \mathbf{0}$, and that diffusion is negligible. Then, Eq. (3) reduces to

$$\partial_t \rho' = s. \quad (7)$$

From Eq. (7) we can then interpret s as the increase rate of density fluctuations at the source. Note that $s < 0$ (i.e., s must be a density reduction rate) to have fluid elements pushed upwards by the buoyancy force. This choice corresponds to a hot source as the equivalent temperature increase rate, $\partial_t \Delta T > 0$, can be estimated from the density variations as $\partial_t \rho' = -\alpha \rho_0 \partial_t \Delta T$, where α is the thermal expansion coefficient and ρ_0 is the mean fluid density.

We want to estimate the potential energy input rate, \dot{E}_p . The total density of the fluid is given by Eq. (4), where we can take $z_0 = 0$ without loss of generality. If the density in the source region (at $z = z_s$) differs from the surrounding atmosphere by $\Delta \rho$, i.e., the density in that region is $\rho_s = \rho_0 + (d\bar{\rho}/dz)z_s + \Delta \rho$, it will be in equilibrium at a height z_{eq} given by

$$\rho_0 + \frac{d\bar{\rho}}{dz}z_s + \Delta \rho = \rho_0 + \frac{d\bar{\rho}}{dz}z_{eq}. \quad (8)$$

Solving this equation we obtain

$$z_{eq} = z_s + \frac{\Delta \rho}{(d\bar{\rho}/dz)}, \quad (9)$$

or alternatively

$$\Delta \rho = \frac{d\bar{\rho}}{dz}(z_{eq} - z_s). \quad (10)$$

In the absence of any other atmospheric fluctuations ($\rho' = 0$ except at the source), the buoyancy force applied to a fluid element with density ρ_s at any given z is

$$[\rho(z) - \rho_s]g = \left[\frac{d\bar{\rho}}{dz}(z - z_s) - \Delta \rho \right]g = \frac{d\bar{\rho}}{dz}(z - z_{eq})g. \quad (11)$$

The potential energy per unit volume in a density variation $\Delta \rho$ at z_s , $e_p = E_p/V_s$ (where V_s is the source volume), is then equal to minus the work required to move the fluid element from z_{eq} to z_s ,

$$e_p = - \int_{z_{eq}}^{z_s} \frac{d\bar{\rho}}{dz}(z - z_{eq})g dz = - \frac{1}{2} \frac{d\bar{\rho}}{dz}(z_s - z_{eq})^2 g. \quad (12)$$

Substituting from Eq. (10),

$$e_p = - \frac{1}{2} \frac{\Delta \rho^2}{(d\bar{\rho}/dz)} g. \quad (13)$$

The potential energy input rate per unit volume is

$$\dot{e}_p = -\Delta \rho \frac{d\Delta \rho}{dt} \frac{g}{(d\bar{\rho}/dz)}. \quad (14)$$

Note that $\Delta \rho = \rho'$ at the source region. As the velocity is negligible there, $d\rho'/dt \approx \partial_t \rho'$. According to Eq. (7), we can then also replace $d\Delta \rho/dt$ by s . Thus,

$$\dot{e}_p = -\rho' s \frac{g}{(d\bar{\rho}/dz)}. \quad (15)$$

Integrating \dot{e}_p over the source volume we finally obtain

$$\dot{E}_p = -\langle \rho' s \rangle \frac{g V_s}{(d\bar{\rho}/dz)} = \varepsilon \rho_0 V_s, \quad (16)$$

where $\varepsilon = -g \langle \rho' s \rangle [\rho_0 (d\bar{\rho}/dz)]^{-1}$ is the potential energy input rate per unit of mass, and the brackets denote the volume average. From the simulations, using $g = 9.8 \text{ m s}^{-2}$ and $\rho_0 = 1.225 \text{ kg m}^{-3}$, then $\varepsilon = 1.2 \text{ W kg}^{-1}$ and $\dot{E}_p \approx 1.6 \times 10^{12} \text{ W}$. This energy release rate is comparable with an eruption with a mass discharge rate of $2 \times 10^8 \text{ kg s}^{-1}$, assuming the heat capacity is 1000 J kg^{-1} and the excess temperature is 800 K .

Data availability

Data in all figures (observed lightning rings, radial profiles of square vorticity and density of particles, radius of the cloud, and power spectra) are available at <https://doi.org/10.5281/zenodo.8417338>⁷¹.

Code availability

The GHOST code used for the simulations, with configuration files and examples, is available at <https://doi.org/10.5281/zenodo.8015308>⁷². Three-dimensional renderings were done with VAPOR, available at <https://doi.org/10.5281/zenodo.7779648>⁷³. Both codes are publicly available and run on most UNIX systems. GHOST is maintained by its authors⁶⁷. VAPOR is a product of the National Center for Atmospheric Research's Computational and Information Systems Lab. Support for VAPOR is provided by the U.S. National Science Foundation and by the Korea Institute of Science and Technology Information^{68,74}.

Received: 3 June 2023; Accepted: 25 October 2023;
Published online: 15 November 2023

References

- Brenna, M. et al. Post-caldera volcanism reveals shallow priming of an intra-oceanic arc andesitic caldera: Hunga volcano, Tonga, SW Pacific. *Lithos* **412–413**, 106614 (2022).
- Colombier, M. et al. Vesiculation and quenching during Surtseyan eruptions at Hunga Tonga-Hunga Ha'apai volcano, Tonga. *J. Geophys. Res.- Solid Earth* **123**, 3762–3779 (2018).
- Cronin, S. J. et al. New volcanic island unveils explosive past. *EOS* **98**, <https://eos.org/science-updates/new-volcanic-island-unveils-explosive-past> (2017).
- Matoza, R. S. et al. Atmospheric waves and global seismoacoustic observations of the January 2022 Hunga eruption, Tonga. *Science* **377**, 95–100 (2022).
- Wright, C. J. et al. Surface-to-space atmospheric waves from Hunga Tonga-Hunga Ha'apai eruption. *Nature* **609**, 741–746 (2022).
- Yuen, D. A. et al. Under the surface: pressure-induced planetary-scale waves, volcanic lightning, and gaseous clouds caused by the submarine eruption of Hunga Tonga-Hunga Ha'apai volcano. *Earthq. Res. Adv.* **2**, 100134 (2022).
- Proud, S. R., Prata, A. T. & Schmauss, S. The January 2022 eruption of Hunga Tonga-Hunga Ha'apai volcano reached the mesosphere. *Science* **378**, 554–557 (2022).
- Jarvis, P. A. et al. Volcanic lightning reveals plume and umbrella cloud dynamics of the January 2022 Hunga Tonga-hunga Ha'apai eruption. *Book of Abstracts, IAVCEI 2023 Scientific Assembly* 522 (2023).
- Kubota, T., Saito, T. & Nishida, K. Global fast-traveling tsunamis driven by atmospheric lamb waves on the 2022 Tonga eruption. *Science* **377**, 91–94 (2022).
- Poli, P. & Shapiro, N. M. Rapid characterization of large volcanic eruptions: measuring the impulse of the Hunga Tonga Ha'apai explosion from teleseismic waves. *Geophys. Res. Lett.* **49**, e2022GL098123 (2022).
- Vergoz, J. et al. IMS observations of infrasound and acoustic-gravity waves produced by the January 2022 volcanic eruption of Hunga, Tonga: a global analysis. *Earth Planet Sci. Lett.* **591**, 117639 (2022).
- Astafeyeva, E. et al. The 15 January 2022 Hunga Tonga eruption history as inferred from ionospheric observations. *Geophys. Res. Lett.* **49**, e2022GL098827 (2022).
- Purkis, S. M. et al. The 2022 Hunga-Tonga megatsunami: near-field simulation of a once-in-a-century event. *Sci. Adv.* **9**, eadf5493 (2023).

14. Bór, J. et al. Responses of the AC/DC global electric circuit to volcanic electrical activity in the Hunga Tonga-hunga Ha'apai eruption on 15 January 2022. *J. Geophys. Res. Atmos.* **128**, e2022JD038238 (2023).
15. Vaisala Xweather. *Total Lightning Statistics 2022, the Annual Lightning Report*. <https://www.xweather.com/annual-lightning-report> (2023).
16. Németh, K. Geoheritage and geodiversity aspects of catastrophic volcanic eruptions: lessons from the 15th of January 2022 Hunga Tonga - Hunga Ha'apai Eruption, SW Pacific. *Int. J. Geoheritage Parks* **10**, 546–568 (2022).
17. Van Eaton, A. R. et al. Lightning rings and gravity waves: Insights into the giant eruption plume from Tonga's Hunga volcano on 15 January 2022. *Geophys. Res. Lett.* **50**, e2022GL102341 (2023).
18. Krehbiel, P. R. et al. GPS-based Mapping system reveals lightning inside storms. *Eos, Trans. Amer. Geophys. Union* **81**, 21–25 (2000).
19. Wiens, K. C., Rutledge, S. A. & Tessendorf, S. A. The 29 June 2000 supercell observed during steps. Part II: Lightning and charge structure. *J. Atmos. Sci.* **62**, 4151–4177 (2005).
20. Cerminara, M., Esposti Ongaro, T. & Neri, A. Large eddy simulation of gas-particle kinematic decoupling and turbulent entrainment in volcanic plumes. *J. Volcanol. Geoth. Res.* **326**, 143–171 (2016).
21. Said, R. K. Towards a global lightning locating system. *Weather* **72**, 36–40 (2017).
22. Nakada, S. et al. Volcanological timeline of the Hunga Tonga-Hunga Ha'apai eruption in mid-January 2022. *Japan Geoscience Union Meeting Abstract U09-07* (2022).
23. Cimarelli, C., Alatorre-Ibargueñoitia, M. A., Kueppers, U., Scheu, B. & Dingwell, D. B. Experimental generation of volcanic lightning. *Geology* **42**, 79–82 (2014).
24. Gaudin, D. & Cimarelli, C. The electrification of volcanic jets and controlling parameters: a laboratory study. *Earth Planet Sci. Lett.* **513**, 69–80 (2019).
25. Harper, J. M., Cimarelli, C., Cigala, V., Kueppers, U. & Dufek, J. Charge injection into the atmosphere by explosive volcanic eruptions through triboelectrification and fragmentation charging. *Earth Planet Sci. Lett.* **574**, 117162 (2021).
26. Prata, A. T. et al. Anak Krakatau triggers volcanic freezer in the upper troposphere. *Sci. Rep.* **10**, 3584 (2020).
27. Van Eaton, A. R. et al. Did ice-charging generate volcanic lightning during the 2016-2017 eruption of Bogoslof Volcano, Alaska? *Bull. Volcanol.* **82**, 24 (2020).
28. Cimarelli, C. & Genareau, K. A review of volcanic electrification of the atmosphere and volcanic lightning. *J. Volcanol. Geoth. Res.* **422**, 107449 (2022).
29. Cimarelli, C., Behnke, S., Genareau, K., Harper, J. M. & Van Eaton, A. R. Volcanic electrification: recent advances and future perspectives. *Bull. Volcanol.* **84**, 78 (2022).
30. Blanchard, D. C. Charge separation from saline drops on hot surfaces. *Nature* **201**, 1164–1166 (1964).
31. Buttner, R., Roder, H. & Zimanowski, B. Electrical effects generated by experimental volcanic explosions. *Appl. Phys. Lett.* **70**, 1903–1905 (1997).
32. Björnsson, S., Blanchard, D. C. & Spencer, A. T. Charge generation due to contact of saline waters with molten lava. *J. Geophys. Res.* **72**, 1311–1323 (1967).
33. Stern, S., Cimarelli, C., Gaudin, D., Scheu, B. & Dingwell, D. B. Electrification of experimental volcanic jets with varying water content and temperature. *Geophys. Res. Lett.* **46**, 11136–11145 (2019).
34. Aizawa, K. et al. Physical properties of volcanic lightning: constraints from magnetotelluric and video observations at Sakurajima volcano, Japan. *Earth Planet Sci. Lett.* **444**, 45–55 (2016).
35. Behnke, S. A. & Bruning, E. C. Changes to the turbulent kinematics of a volcanic plume inferred from lightning data. *Geophys. Res. Lett.* **42**, 4232–4239 (2015).
36. Cimarelli, C. et al. Multiparametric observation of volcanic lightning: Sakurajima volcano, Japan. *Geophys. Res. Lett.* **43**, 4221–4228 (2016).
37. Falkovich, G., Fouxon, A. & Stepanov, M. G. Acceleration of rain initiation by cloud turbulence. *Nature* **419**, 151–154 (2002).
38. Mehlig, B., Uski, V. & Wilkinson, M. Colliding particles in highly turbulent flows. *Phys. Fluids* **19**, 098107 (2007).
39. Wilkinson, M. & Mehlig, B. Caustics in turbulent aerosols. *Europhys. Lett.* **71**, 186–192 (2005).
40. Morton, B. R., Taylor, G. I. & Turner, J. S. Turbulent gravitational convection from maintained and instantaneous sources. *Proc. Royal Soc. A: Math. Phys. Eng. Sci.* **234**, 1–23 (1956).
41. Costa, A. et al. Results of the eruptive column model inter-comparison study. *J. Volcanol. Geotherm. Res.* **326**, 2–25 (2016).
42. Hunt, G. R. & Van Den Bremer, T. S. Classical plume theory: 1937–2010 and beyond. *IMA J. Appl. Math.* **76**, 424–448 (2011).
43. Mastin, L. G. A user-friendly one-dimensional model for wet volcanic plumes. *Gochem. Geophys. Geosys.* **8**, Q03014 (2007).
44. Woods, A. The fluid-dynamics and thermodynamics of eruption columns. *Bull. Volcanol.* **50**, 169–193 (1988).
45. Woods, A. & Kienle, J. The dynamics and thermodynamics of volcanic clouds - theory and observations from the April 15 and April 21, 1990 eruptions of Redoubt Volcano, Alaska. *J. Volcanol. Geotherm. Res.* **62**, 273–299 (1994).
46. Ogden, D. E., Glatzmaier, G. A. & Wohletz, K. H. Effects of vent overpressure on buoyant eruption columns: implications for plume stability. *Earth Planet Sci. Lett.* **268**, 283–292 (2008).
47. Ogden, D. E., Wohletz, K. H., Glatzmaier, G. A. & Brodsky, E. E. Numerical simulations of volcanic jets: importance of vent overpressure. *J. Geophys. Res.* **113**, B02204 (2008).
48. Wilson, L., Sparks, R. S. J., Huang, T. C. & Watkins, N. D. The control of volcanic column heights by eruption energetics and dynamics. *J. Geophys. Res.* **83**, 1829–1836 (1978).
49. Bursik, M. Effect of wind on the rise height of volcanic plumes. *Geophys. Res. Lett.* **28**, 3621–3624 (2001).
50. de' Michieli Vitturi, M., Engwell, S. L., Neri, A. & Barsotti, S. Uncertainty quantification and sensitivity analysis of volcanic columns models: results from the integral model plume-mom. *J. Volcanol. Geoth. Res.* **326**, 77–91 (2016).
51. Koyaguchi, T. & Woods, A. W. On the formation of eruption columns following explosive mixing of magma and surface-water. *J. Geophys. Res.-Solid Earth* **101**, 5561–5574 (1996).
52. Maeno, F. et al. Seawater-magma interactions sustained the high column during the 2021 phreatomagmatic eruption of Fukutoku-Oka-no-Ba. *Comm Earth Envi.* **3**, 260 (2022).
53. Cerminara, M., Esposti Ongaro, T. & Berselli, L. C. ASHEE-1.0: a compressible, equilibrium-Eulerian model for volcanic ash plumes. *Geosci. Model Dev.* **9**, 697–730 (2016).
54. Esposti Ongaro, T. & Cerminara, M. Non-equilibrium processes in ash-laden volcanic plumes: new insights from 3d multiphase flow simulations. *J. Volcanol. Geoth. Res.* **326**, 127–142 (2016).
55. Suzuki, Y. J. et al. Inter-comparison of three-dimensional models of volcanic plumes. *J. Volcanol. Geotherm. Res.* **326**, 26–42 (2016).
56. Suzuki, Y. J. & Iguchi, M. Determination of the mass eruption rate for the 2014 Mount Kelud eruption using three-dimensional numerical simulations of volcanic plumes. *J. Volcanol. Geotherm. Res.* **382**, 42–49 (2019).
57. Hernandez-Duenas, G., Majda, A. J., Smith, L. M. & Stechmann, S. N. Minimal models for precipitating turbulent convection. *J. Fluid Mech.* **717**, 576–611 (2013).
58. Di Renzo, M. & Urzay, J. Aerodynamic generation of electric fields in turbulence laden with charged inertial particles. *Nat. Commun.* **9**, 1676 (2018).
59. Dash, J. G., Mason, B. L. & Wettlaufer, J. S. Theory of charge and mass transfer in ice-ice collisions. *J. Geophys. Res. Atmos.* **106**, 20395–20402 (2001).
60. Saunders, C. P. R. & Peck, S. L. Laboratory studies of the influence of the rime accretion rate on charge transfer during graupel/crystal collisions. *J. Geophys. Res.* **103**, 13949–13956 (1998).
61. Takahashi, T. Riming electrification as a charge generation mechanism in thunderstorms. *J. Atmos. Sci.* **35**, 1536–1548 (1978).
62. Van Aartrijk, M. & Clercx, H. J. H. The dynamics of small inertial particles in weakly stratified turbulence. *J. Hydro-Environ. Res.* **4**, 103–114 (2010).
63. Kintner, J. A., Yeck, W. L., Earle, P. S., Prejean, S. & Pesicek, J. D. High-precision characterization of seismicity from the 2022 Hunga Tonga-Hunga Ha'apai volcanic eruption. *Seismol. Res. Lett.* **94**, 589–602 (2022).
64. Basu, S. & Holtslag, A. A. M. Turbulent Prandtl number and characteristic length scales in stably stratified flows: steady-state analytical solutions. *Environ. Fluid Mech.* **21**, 1273–1302 (2021).
65. Maxey, M. & Riley, J. Equation of motion for a small rigid sphere in a nonuniform flow. *Phys. Fluids* **26**, 883–889 (1983).
66. Good, G. H. et al. Settling regimes of inertial particles in isotropic turbulence. *J. Fluid Mech.* **759**, R3 (2014).
67. Mininni, P. D., Rosenberg, D., Reddy, R. & Pouquet, A. A hybrid MPI-OpenMP scheme for scalable parallel pseudospectral computations for fluid turbulence. *Parallel Comput.* **37**, 316–326 (2011).
68. Clyne, J., Mininni, P., Norton, A. & Rast, M. Interactive desktop analysis of high resolution simulations: application to turbulent plume dynamics and current sheet formation. *New J. Phys.* **9**, 301 (2007).
69. Vallis, G. K. *Atmospheric and Oceanic Fluid Dynamics* (Cambridge University Press, 2017).
70. Angriman, S. et al. Clustering in laboratory and numerical turbulent swirling flows. *J. Fluid Mech.* **948**, A30 (2022).
71. Mininni, P. D., Ichihara, M., Ravichandra, S., Cimarelli, C. & Vagasky, C. Dataset for multiphase turbulent flow explains lightning rings in volcanic plumes. <https://doi.org/10.5281/zenodo.8417338> (2023).
72. Rosenberg, D., Mininni, P. D. & Clark Di Leoni, P. pmininni/GHOST: GHOST master. <https://doi.org/10.5281/zenodo.8015308> (2023).
73. Pearse, S. et al. NCAR/VAPOR: Vapor 3.8.1. <https://doi.org/10.5281/zenodo.7779648> (2023).
74. Li, S., Jaroszynski, S., Pearse, S., Orf, L. & Clyne, J. Vapor: a visualization package tailored to analyze simulation data in earth system science. *Atmosphere* **10**, 488 (2019).

Acknowledgements

This research was initiated by the discussion at “Multiphase Flows in Geophysics and the Environment” program of KITP supported by the National Science Foundation under Grant No. NSF PHY-1748958. The authors thank the program coordinators (Elisabeth Guazzelli, Michael Manga, Eckart Meiburg, and Raymond Shaw) for giving us the opportunity to attend. M.I. participated in the program partly supported by JSPS KAKENHI (No. JP19H00713) and proceeded the research funded by JSPS KAKENHI (No. 21K21353). S.R. acknowledges travel funding from Oracle Inc. under grant DO/2022-ORFS002-001 that enabled his visit to KITP. P.D.M. acknowledges support from PICT Grant No. 2018-4298. C.C. acknowledges funding from ERC-Con Grant “VOLTA” under contract N° 864052. The authors thank Vaisala for providing access to the GLD360 data through their research data grant program, and thank Takayuki Kaneko and Takuro Horiuchi for supporting satellite image processing. The authors are grateful to Joe Aslin, Senior Editor of Communications Earth & Environment, and three anonymous reviewers who helped improve the manuscript.

Author contributions

M.I. and P.D.M. conceived the presented idea. P.D.M. performed the computations and data analysis. S.R. contributed theoretical ideas for this work. C.C. oversaw the study from the perspective of volcanic lightning research. M.I. and C.C. performed analysis of observational data. C.V. contributed GLD360 lightning data and provided help with data analysis. All authors discussed the results and contributed to the final manuscript.

Competing interests

The authors declare no competing interests.

Additional information

Supplementary information The online version contains supplementary material available at <https://doi.org/10.1038/s43247-023-01074-z>.

Correspondence and requests for materials should be addressed to Mie Ichihara.

Reprints and permission information is available at <http://www.nature.com/reprints>

Publisher's note Springer Nature remains neutral with regard to jurisdictional claims in published maps and institutional affiliations.



Open Access This article is licensed under a Creative Commons Attribution 4.0 International License, which permits use, sharing, adaptation, distribution and reproduction in any medium or format, as long as you give appropriate credit to the original author(s) and the source, provide a link to the Creative Commons licence, and indicate if changes were made. The images or other third party material in this article are included in the article's Creative Commons licence, unless indicated otherwise in a credit line to the material. If material is not included in the article's Creative Commons licence and your intended use is not permitted by statutory regulation or exceeds the permitted use, you will need to obtain permission directly from the copyright holder. To view a copy of this licence, visit <http://creativecommons.org/licenses/by/4.0/>.

© The Author(s) 2023